Daily changes of seismic velocities in shallow materials on Mars

Lei Qin[1], Hongrui Qiu[2], Sizhuang Deng[2], Alan Levander[2] and Yehuda Ben-Zion[1,3]

[1]Department of Earth Sciences, University of Southern California, Los Angeles, CA, USA

[2]Department of Earth, Environmental and Planetary Sciences, Rice University, Houston, TX, USA

[3]Southern California Earthquake Center, University of Southern California, Los Angeles, CA, USA

Corresponding author: Lei Qin (qinl@usc.edu)

Key points:

- Reflection phases are seen at ~1.2 s, ~2.4 s, and ~3.9 s in autocorrelations of the InSight seismic data for all three components
- Daily velocity variations averaged in the top ~18-200 m of ~40-5% are resolved using reflection waves at ~4 Hz
- The changes are driven by surface temperature variations producing thermoelastic strain and material failure at shallow depth

Abstract

Temporal changes of S-wave velocities at shallow depth on Mars are derived using seismic data from the InSight mission. Autocorrelation functions are computed for three-component seismic recordings to retrieve zero-offset reflection seismograms. Observed S-wave reflection phase with two-way travel time of ~1.2 s and its multiples indicate an interface at ~200 m depth. Daily relative travel time changes (dt/t) with ~5% variations are correlated well with the surface temperature. A top ~1m-thick regolith layer produces a delay of about one Martian day between the dt/t and surface temperature. Assuming the travel time changes are produced primarily in the top ~18 m sand layer, the daily velocity variations in that layer are ~40%. The dominant mechanisms driving the changes are thermoelastic strain in the shallow structure generating the time delays and possible material failures in the regolith layer.

Plain Language Summary

Seismic and environmental data provided by the InSight mission are used to study the behavior of shallow materials on Mars in response to daily temperature variations. Autocorrelations of moving time windows of the seismic data provide information on waves that are excited and recorded at the sensor location. Signals reflected at an interface ~200 m deep with ~5% daily travel time variations are seen in the autocorrelations. The travel time variations correlate well with the surface temperature data. A delay of about one Martian day may be generated by the ~1m-thick unconsolidated surface layer on Mars. The analysis suggests that the changes of travel times are produced by thermal-induced strain and related perturbations to elastic moduli and mass density in the shallow structure on Mars. If the observed ~5% daily travel time variations are concentrated in the top ~18 m sand layer, there are ~40% corresponding daily velocity variations in the layer.

1. Introduction

Seismic interferometry has been widely used to image (Lin et al., 2013; Phạm & Tkalčić, 2017; Romero & Schimmel, 2018; Shapiro & Campillo, 2004) and monitor buildings and seismic structures on Earth (e.g. Bonilla et al., 2019; Brenguier et al., 2008; Mao et al., 2019; Prieto et al., 2010; Qin et al., 2020). Velocity variations associated with earthquakes (e.g. Karabulut & Bouchon, 2007; Peng & Ben-Zion, 2006) and periodic (e.g. daily, seasonal) loadings such as hydrological changes, thermoelastic strain and tides (Ben-Zion & Allam, 2013; Johnson et al., 2017; Mao et al., 2019), shed light on in-situ structures and susceptibility of subsurface materials to failure. These issues are of great importance to interpreting observed seismic motion, reliability of underground facilities and other applications.

Recent developments enabled geophysical studies on Mars and other objects in the solar system. Martian interior structures can be divided (e.g. Fei, 2013; Khan et al., 2018; Yoder et al., 2003) as on Earth into crust, mantle and core (Smrekar et al., 2019). The NASA's Interior Exploration using Seismic Investigations, Geodesy and Heat Transport (InSight) mission deployed a seismic station on Mars at the end of 2018 (Lognonné et al., 2019; Panning et al., 2017). Seismic waveforms from a single three-component station, augmented by environmental data (e.g. Temperature and Wind for InSight (TWINS)), were used to search for marsquake (Banerdt et al., 2020; Giardini et al., 2020), constrain shallow elastic and anelastic properties of Mars (Lognonné et al., 2020), and analyze source properties of the ambient seismic noise on Mars (e.g. Suemoto et al., 2020).

Using seismic interferometry, Deng & Levander (2020) identified prominent body-wave reflection phases in stacked vertical component autocorrelation data, and associated them with reflections from deep interfaces (e.g. the Martian Moho and core-mantle boundary). Analysis of data from the Apollo Lunar Seismic Profiling Experiment (Nakamura et al., 1982) resolved the structures and thermal properties of the Moon (Kovach & Watkins, 1973; Langseth et al., 1976; Larose et al., 2005; Tanimoto et al., 2008) and discovered moonquakes triggered by diurnal temperature changes (Cooper & Kovach, 1975; Duennebier, 1976; Duennebier & Sutton, 1974).

In this study, we retrieve high-frequency (~4 Hz) body waves reflected from a shallow (~200 m deep) interface using moving short-time (20 s) window autocorrelations of seismic recordings, and analyze daily variations in arrival times of the reflections to monitor possible material changes in near-surface structures. Considering the large daily temperature variations (~76ºC) and low barometric pressure (~700 Pa) on Mars, the in-situ monitoring of velocity variations aims to provide high-resolution information on the properties and dynamics of the shallow materials at the study area on Mars.

2. Data & Instrumentation

NASA's InSight spacecraft deployed a six-axis seismometer on Mars providing seismic data sampled at 10 Hz, 20 Hz and 100 Hz, augmented by the TWINS environmental sensors. Except for the detected marsquakes (Giardini et al., 2020), seismic data on Mars are dominated by noise from atmospheric events and wind-generated lander noise (Lognonné et al., 2020; Suemoto et al., 2020). Surficial geology studies (Golombek et al., 2020) and investigation of seismic data (Lognonné et al., 2020) at the landing site suggest a relatively smooth terrain with a ~3-18m-thick layer of sand with few rocks overlying coarse breccia. Analyses of seismic and environmental recordings on Mars (Lognonné et al., 2020) provided near-surface Young's modulus (~47 MPa), P-wave velocity (118±34 m/s) and thermal inertia (160-230 $Jm^{-2}K^{-1}s^{-1/2}$) of the regolith layer in the top 1-2 m.

We analyze the seismic and environmental data (Fig. 1) for temporal variations in the properties of near-surface structures on Mars. The 100 Hz seismic data are continuously recorded during Julian days 66-67 (UTC on Earth; Fig. S1); therefore, we present the analysis primarily based on the two-day 100 Hz data. Close to this time interval, the 20 Hz (days 63-65) data are also analyzed (supporting information) to show similar patterns with those derived from the 100 Hz data but with larger uncertainties. Temperature and wind recordings are plotted in Figs 1&S2. The three-component recordings are detrended and rotated to the geographical east-west (EW), north-south (NS), and vertical (UD) components (e.g. Fig. 1a). The rotated data are then segmented into 20s-long time windows with 50% overlap, resulting in analysis time steps of 10 s. The daily amplitude variations of seismic data are significant (~3 orders of magnitude) at frequencies above ~5 Hz, as is shown in Figs 1b&S3. Thus, for each time window, we bandpass filter the data at 1-5 Hz, where the amplitude variation is less dramatic, and calculate autocorrelation functions (ACFs) to retrieve the zero-offset reflection seismograms. Resulting ACFs are presented in Figs 2&S4-S5. By tracking travel time variations of body waves in ACFs reflected from interfaces beneath the station, we can infer the temporal evolution of subsurface materials at the InSight landing site.

For each ACF, the delay of travel time (dt) with respect to a reference trace associated with the stack of all ACFs is obtained through cross-correlation in a time window where clear reflected phases are observed. Fig. 2c shows the reference ACFs (black dashed curves) and example traces (black solid curves) at 1 pm of Julian day 66. The cross-correlation time window is determined as follows: (i) We first stack the envelopes of all ACFs (Figs 2&S4-S5), and center the cross-correlation time window at the second peak (i.e. the highest peak excluding the zero-lag) of the stacked envelope function (Figs 2d&S6). (ii) Then we calculate the dominant frequency for each trace and remove ACFs with peak frequencies that are larger than 5 Hz or lie outside three times the standard deviation in the distribution of ACF dominant frequencies (Fig. S7). The obtained median dominant frequency f_0 is ~4 Hz, close to the Nyquist frequency of the 10 Hz data, therefore the analyses based on 10 Hz data are less reliable and not presented in this paper. (iii) The cross-correlation time window is defined as ±3 times the median dominant period $T_0 = 1/f_0$ from the center determined in step (i), resulting in ~1.5s-long cross-correlation time windows (blue vertical lines in Fig. 2c)

We show the stacked envelope functions and cross-correlation time windows in Fig. 2d for the three components at 100 Hz and in Fig. S6 for data at 20 Hz. To suppress potential effects of wavefield changes on the inferred delay times, we discard the ACF if any of the following holds: (i) The peak value of envelope function in the cross-correlation time window is smaller than 20% quantile of the peak envelope values from all ACFs. (ii) The cross-correlation coefficient with the reference ACF trace is less than 0.5. (iii) The retrieved dt deviates more than three times the median absolute deviation from the median.

3. Analysis

The travel time variations are clearly seen in the two-day EW-component ACFs filtered at 1-5 Hz from the 100 Hz data (Fig. 2a). Results for the other two components (Fig. S4) and data at 20 Hz (Fig. S5) show consistent patterns. Reflected signals at ~1.2 s, ~2.4 s, and 3.9 s (i.e. two-way travel time) are observed in the stacked envelope functions (e.g. Fig. 2d). The cross-correlation time windows used to calculate delay time are centered on the first labeled peak, T_1 = 1.17 s, 1.29 s, 1.19 s for EW, NS and UD components, respectively. The relative travel time change averaged over the entire propagation path is calculated as dt/t, where t is the lapse time for the center of the cross-correlation time window. Positive dt/t values indicate increasing travel time and thus slower seismic velocities.

Fig. 3 shows the observed dt/t values colored by the cross-correlation coefficients, estimated from the two-day 100 Hz data. Due to the large scattering of the observed dt/t values, we smooth the measurements by taking the running median for every 65 points, and calculate the corresponding standard deviation as the data uncertainty (gray area in Fig. S8). The smoothed dt/t curve has a maximum time resolution of ~10 min. We choose a window size of 65 points due to the trade-off between time resolution and smoothness of the resulting dt/t curve. Spikes still present in the smoothed dt/t data (e.g. red curves in Fig. 3) and are likely associated with data gaps and low-quality ACFs (e.g. Fig. 2a). Results from the 20 Hz data are illustrated in Fig. S9 (results for the NS component are not shown due to low data quality).

The smoothed dt/t curves (e.g. Fig. 3) have a similar shape to the temperature recording (Fig. 1c), showing a relatively flat linear change during Martian night times (e.g. 8:00 pm to 8:00 am) and significant variations during the daytime (e.g. 8:00 am to 8:00 pm; between the purple dashed lines in Fig. 3). This is in contrast to the more complicated pattern of wind recordings (Fig. 1c) and indicates that the dominant mechanism driving the temporal change is associated with temperature. Since high frequency (>1 Hz) seismic noise recorded at the site is dominated by wind-induced lander noise (e.g. Suemoto et al., 2020), the contribution from wavefield changes to the resolved dt/t curves is negligible. We compare the smoothed dt/t curve with a linear transformation of the temperature recording $T(t)$ given by $g_0(T; a, b) = a \cdot T(t) + b$. The coefficients $a > 0$ and b are determined so that the maximum and minimum values of the $g_0(T; a, b)$ match, respectively, the median values of the upper 95 and lower 5 percentiles of the smoothed dt/t curve. The obtained a and b parameters are presented in Table S1 and show consistent values from different data sets.

The difference between the linearly-scaled temperature (black curve) and smoothed dt/t values (red curve) in Fig. 3, $\delta_0(t) = g_0(T; a, b) - dt/t$, is much smaller than the data uncertainties (shaded area in Fig. S8) during Martian night times (e.g. 8:00 pm to 8:00 am). This indicates a robust linear relation between the smoothed dt/t and surface temperature (hereinafter, dt/t-temperature relation). We also find a good agreement in the timing between the two curves of the turning point around 6 am in the Martian time, after which the temperature and dt/t values increase dramatically. This suggests the time delay between the smoothed dt/t curve and surface temperature is comparable to the time resolution of the data (~10 min) at Martian night plus possible multiples of Martian day. The difference $\delta_0(t)$ during the Martian daytime (e.g. between the purple dashed lines in Fig. 3) is much larger than that at night, indicating either a nonlinear relation or a different time shift between these two curves during the daytime. The same dt/t-temperature relations are also consistently observed in data at 20 Hz (Fig. S9).

We further verify the robustness of the observed dt/t-temperature relation through curve fitting the smoothed dt/t using $g_0(T; a, b)$, i.e. inferring the coefficients a and b by minimizing $\delta_0(t)^2$ for all available data. The best fitting result (black curve in the upper panel of Fig. S10) shows that we cannot fit the measurements equally well during the Martian night and day times. We also conduct the curve fitting using $g_1(T; a, b, t_0) = a \cdot T(t - t_0) + b$, considering possible time shift t_0 between the two curves. The best fitting result is obtained by minimizing $\delta_1(t; t_0)^2$ for each possible t_0 from -2 h to 2 h, where $\delta_1(t; t_0) = g_1(T; a, b, t_0) - dt/t$. We note that the estimated time shift t_0 is representative of the wrapped phase delay and may be cycle skipped, i.e. the actual delay is $t_d = t_0 + T_M \cdot N$, where *N* is an integer and T_M is a Martian day. The result indicates the best fitting t_0 is -45 mins (bottom panel of Fig. S10), when all available dt/t data are used, implying that the smoothed dt/t curve likely either precedes the temperature record by ~45 min or is delayed by ~23 hours. Considering the best fitting $\delta_1(t; t_0)$ is smaller than the data uncertainties (shaded area in Fig. S8), we rule out the possibility of a non-linear dt/t-temperature relation during Martian day times. The best fitting time shift t_0 remains negative for all data sets, and the absolute value becomes smaller when $\delta_1(t;t_0)^2$ is minimized during Martian night times (e.g. 8:00 pm to 8:00 am) and larger when $\delta_1(t;t_0)^2$ is minimized during Martian day times (e.g. 8:00 am to 8:00 pm). The time delay from the curve fitting suggests the actual delay t_d between the dt/t curve and the temperature record is smaller during the day times.

In general, the curve fitting results are less reliable because of possible trade-offs between parameters. Therefore, we only focus below on the comparison between the smoothed dt/t data and $g_0(T;a,b)$ shown as black curve in Fig. 3. Since $g_0(T;a,b)$ represents dt/t if it is linearly related to the surface temperature with a negligible wrapped phase delay, the absolute difference, $|\delta_0(t)|$, is large when a different wrapped phase delay exists. The relatively large absolute values of $\delta_0(t)$ during the daytime (between the purple dashed lines in Fig. 3) imply variations of phase delay between dt/t and surface temperature. Results from 20 Hz data show similar trends (Fig. S9). We also investigate the temporal pattern of dt/t for potential long-term variations using the 20 Hz data between Julian days 153-365 in 2019. However, except for the observed daily changes, we do not find any linear or periodic long-term patterns that stand out from the background fluctuations.

4. Discussion

We monitor temporal changes of seismic velocities in subsurface materials beneath the InSight lander on Mars using reflected body waves resolved from autocorrelation functions (ACFs) of ambient seismic noise recordings. The stacked envelope function (e.g. Fig. 2d) shows peaks at ~1.2 s, ~2.4 s and ~3.9 s for all three components. It is important to note that there are no clear signals at ~0.6 s, ~1.8 s or ~3.0 s in the stacked envelope function, suggesting the first arriving phase has a two-way travel time of ~1.2 s with the later phases being its multiples. Based on the polarization analysis of Suemoto et al. (2020), P and S reflected waves at the InSight landing site are identified in ACFs with two-way travel times of ~0.6 s and ~1.2 s, respectively. This suggests the observed phase at ~1.2 s and its multiples in the horizontal component ACFs are *S*-wave reflections.

The first arriving reflected phase resolved in ACFs of the vertical component also yields a two-way travel time of ~1.2 s (blue curve in Fig. 2d). This is likely due to the leakage of S wave energy onto the vertical component (e.g. Deng & Levander, 2020; Gorbatov et al., 2013; Oren & Nowack, 2017; Phạm & Tkalčić, 2017). Another possibility is that the first arriving phase in the vertical component travels as P waves in the regolith layer (~1-2 m thick; Lognonné et al., 2020), and converts to S waves at depth. We therefore attribute the dt/t values measured from all three components to temporal changes in *S*-wave travel times.

We use the *S*-wave velocity model A1 from Lognonné et al. (2020), where the *S*-wave velocity increases from 59.85 m/s to 95.82 m/s in the top 1 m, and remains 316.23 m/s between 1-10 m, to estimate the depth of the reflection interface. Assuming the same *S*-wave velocity of 316.23 m/s for structures below 10 m, the two-way travel time of ~1.2 s corresponds to a reflector at a depth of ~200 m. To infer the structural perturbations responsible for the observed travel time variations, the relative velocity change dv/v can be estimated via $dv/v = -dt/t$ (e.g. Ratdomopurbo & Poupinet, 1995; Snieder et al., 2002) by assuming a homogeneous medium change. This results in a ~5% daily maximum variations in *S*-wave velocity averaged over the top ~200 m.

However, the assumption of a homogenous dv/v in subsurface structures is unrealistic and the changes are likely to concentrate in the very shallow damaged materials. The material strength increases with confining pressure so shallow materials are more susceptible to failure (Nur & Simmons, 1969; Yang et al., 2019). In addition, laboratory experiments (e.g. Pasqualini et al., 2007; TenCate et al., 2004) show that shallow soft materials (e.g. soil) exhibit high susceptibility to loading and behave nonlinearly for dynamic strains as low as 10^{-8}, while the strain level needed to generate velocity variations for hard bedrock is considerably larger, on the order of 10^{-3}. Indeed, analysis of borehole data on Earth show that temporal changes tend to concentrate in the top few tens of meters (e.g. Bonilla et al., 2019; Qin et al., 2020; Rubinstein, 2011). Therefore, the dv/v is likely much larger than 5% in the shallow soft materials.

The observed travel time variations dt/t match well with the linearly scaled surface temperature (Fig. 3) with different wrapped phase delays during Martian day (8:00 am to 8:00 pm) and night (8:00 pm to 8:00 am) times, implying the dominant mechanism generating the travel time variations are temperature changes. Thermoelastic strain in an elastic half space covered by an unconsolidated layer is expected to have a phase delay of $\Delta t = \frac{y_b}{2}\sqrt{\frac{\tau}{\pi\cdot\kappa}} + \frac{\tau}{8}$ with respect to the daily variation of surface temperature (Ben-Zion & Leary, 1986; Berger, 1975; Tsai, 2011), where y_b and κ are the thickness and thermal diffusivity of the top incompetent layer and $\tau = 24$ hour. Using for example $y_b = 1$ m (thickness of the regolith layer; Lognonné et al., 2020) and $\kappa = 10^{-6}$ m^2/s (Berger, 1975), Δt is ~26 hours. This delay would be somewhat different if the layer thickness or thermal diffusivity have different values. Using Δt of ~26 hours as the reference, we can unwrap the time delay t_0 resolved between the temperature and smoothed dt/t data in section 3 giving a time delay t_d of ~23 hours during Martian day times and ~24 hours during Martian night times. This is based on the assumption that the clocks of the seismic and thermal sensors are synchronized and thermoelastic strain is the dominating mechanism. Keeping the thermal diffusivity as 10^{-6} m^2/s, the thickness of unconsolidated layer is ~0.9 m to account for the 24-hour delay. This is similar to values of unconsolidated layer thickness inferred from analyses of thermoelastic strain on earth (Ben-Zion & Allam, 2013; Ben-Zion & Leary, 1986; Prawirodirdjo et al., 2006; Wang et al., 2020).

In addition to increasing the delay time for thermoelastic strain, a regolith layer with a thickness in the range of 0.5-1 m (Lognonné et al., 2020) contributes to the observed dt/t through additional thermal related responses, such as changes in mass density and elastic moduli due to crack opening-closing. It is important to note that the time delay t_d is ~1 hour smaller during the Martian day times. Since the delay is smaller for shallower materials within the top layer, the smaller t_d during the day times is likely related to a higher fraction of contribution from the regolith layer to the observed dt/t. This may include material failure due to thermal cracking generated by the significant temperature gradient during the Martian day times. We note that earthquake-like pulses can be generated from thermal cracking in shallow materials, as observed in seismic recordings on the Moon (Tanimoto et al., 2008). In general, thermal-related moonquakes have magnitudes less than −2.0 (Cooper & Kovach, 1975). Since the temperature variations on Mars are smaller than on the Moon, the thermal-related quake-like pulses are excepted to be smaller than those on the Moon. Wind shaking obstacles above the ground (e.g. rocks) can also produce quake-like signals (Johnson et al., 2019). These and other possible environmental sources should be considered when looking for marsquakes.

The sand layer beneath the InSight lander is ~3-18 m thick (Golombek et al., 2020). Based on the velocity model of Lognonné et al. (2020), the S-wave travel time in the top 18 m is ~0.07 s. For simplicity, we use a sand layer thickness of 18 m and neglect the structural perturbations in bedrocks below 18 m. The daily peak to peak fluctuation in S-wave dv/v averaged over the top 18 m sand layer is up to ~40% to account for the 5% daily variaion in the observed dt/t (i.e. ~0.03 s in time delay). This velocity perturbation in response to surface temperature variations on Mars is significantly larger than those resolved on Earth, and may result from the combined effects of extreme environmental conditions (low barometric pressure of ~700 Pa and large temperature variation of ~76ºC) and in-situ structures with extremely low S-wave velocities of <100 m/s in the top 1 m (Lognonné et al., 2020).

5. Conclusions

We monitor temporal variations of seismic velocities on Mars using zero-offset reflection seismograms constructed via short time window autocorrelation of seismic data from the InSight mission. The stacked envelopes of ACFs show clear reflected S waves in three components at ~1.2 s, ~2.4 s, and ~3.9 s. The first arriving phase is reflected from an interface at ~200 m depth based on the local S-wave velocity model (Lognonné et al., 2020), and the later arrivals are its multiples. The maximum delay in the two-way travel time of the first arriving phase is ~0.06 s, corresponding to a relative travel time variation (dt/t) of ~5% averaged over the top ~200 m. The dt/t pattern correlates well with the local surface temperature recording with a phase delay of about one day, suggesting the major mechanisms for the observed temporal variations are thermoelastic strain in the ~18 m sand layer above the bedrock and additional thermal effects such as changes in mass density and elastic moduli in the top 0.5-1 m regolith layer. Sharp temperature increases can introduce thermal cracking near the surface, which contributes to the ~1 hour decrease in time delay between the observed dt/t and linearly scaled temperature data during the Martian day times. The high susceptibility of the damaged materials in the top ~18 m and shallow concentration of the driving mechanisms suggest up to ~40% *S*-wave velocity perturbation in the top ~18 m at the time of the highest temperature on Mars.

Acknowledgements

The InSight seismic data are available through the Incorporated Research Institutions for Seismology (IRIS) data center (InSight Mars SEIS Data Service, 2019; www.iris.edu/hq/sis/insight). The wind and temperature data are downloaded from https://atmos.nmsu.edu/data_and_services/atmospheres_data/INSIGHT/insight.html#Selecting_Data. The study was supported by the U.S. Department of Energy (award DE-SC0016520).

References

Banerdt, W. B., Smrekar, S. E., Banfield, D., Giardini, D., Golombek, M., Johnson, C. L., et al. (2020). Initial results from the InSight mission on Mars. *Nature Geoscience*, *13*(3), 183–189. https://doi.org/10.1038/s41561-020-0544-y

Ben-Zion, Y., & Allam, A. A. (2013). Seasonal thermoelastic strain and postseismic effects in Parkfield borehole dilatometers. *Earth and Planetary Science Letters*, *379*, 120–126. https://doi.org/10.1016/j.epsl.2013.08.024

Ben-Zion, Y., & Leary, P. (1986). Thermoelastic strain in a half-space covered by unconsolidated material. *Bulletin of the Seismological Society of America*, *76*(5), 1447–1460.

Berger, J. (1975). A Note on Thermoelastic Strains and Tilts. *Journal of Geophysical Research*, *80*(2), 274–277.

Bonilla, L. F., Guéguen, P., & Ben-Zion, Y. (2019). Monitoring coseismic temporal changes of shallow material during strong ground motion with interferometry and autocorrelation. *Bulletin of the Seismological Society of America*, *109*(1), 187–198. https://doi.org/10.1785/0120180092

Brenguier, F., Shapiro, N. M., Campillo, M., Ferrazzini, V., Duputel, Z., Coutant, O., & Nercessian, A. (2008). Towards forecasting volcanic eruptions using seismic noise. *Nature Geoscience*, *1*(2), 126–130. https://doi.org/10.1038/ngeo104

Cooper, M. R., & Kovach, R. L. (1975). Energy, frequency, and distance of moonquakes at the Apollo 17 site. *Proc. Lunar Sci. Conf. 6th*, 2863–2879.

Deng, S., & Levander, A. (2020). Autocorrelation Reflectivity of Mars. *Geophysical Research Letters*, *47*. https://doi.org/10.1029/2020GL089630

Duennebier, F. (1976). Thermal movement of the regolith. *Proc. Lunar Sci. Conf. 7th*, 1073–1086.

Duennebier, F., & Sutton, G. H. (1974). Thermal moonquakes. *Journal of Geophysical Research*, *79*(29), 4351–4363. https://doi.org/10.1029/jb079i029p04351

Fei, Y. (2013). Simulation of the planetary interior differentiation processes in the laboratory. *Journal of Visualized Experiments : JoVE*, (81), 1–10. https://doi.org/10.3791/50778

Giardini, D., Lognonné, P., Banerdt, W. B., Pike, W. T., Christensen, U., Ceylan, S., et al. (2020). The seismicity of Mars. *Nature Geoscience*, *13*(3), 205–212. https://doi.org/10.1038/s41561-020-0539-8

Golombek, M., Warner, N. H., Grant, J. A., Hauber, E., Ansan, V., Weitz, C. M., et al. (2020). Geology of the InSight landing site on Mars. *Nature Communications*, *11*(1), 1–11. https://doi.org/10.1038/s41467-020-14679-1

Gorbatov, A., Saygin, E., & Kennett, B. L. N. (2013). Crustal properties from seismic station autocorrelograms. *Geophysical Journal International*, *192*(2), 861–870. https://doi.org/10.1093/gji/ggs064

Johnson, C. W., Fu, Y., & Bürgmann, R. (2017). Stress Models of the Annual Hydrospheric, Atmospheric, Thermal, and Tidal Loading Cycles on California Faults: Perturbation of Background Stress and Changes in Seismicity. *Journal of Geophysical Research: Solid Earth*, *122*(12), 10,605-10,625. https://doi.org/10.1002/2017JB014778

Johnson, C. W., Meng, H., Vernon, F., & Ben-Zion, Y. (2019). Characteristics of Ground Motion Generated by Wind Interaction With Trees, Structures, and Other Surface Obstacles. *Journal of Geophysical Research: Solid Earth*. https://doi.org/10.1029/2018JB017151

Karabulut, H., & Bouchon, M. (2007). Spatial variability and non-linearity of strong ground motion near a fault. *Geophysical Journal International*, *170*(1), 262–274. https://doi.org/10.1111/j.1365-246X.2007.03406.x

Khan, A., Liebske, C., Rozel, A., Rivoldini, A., Nimmo, F., Connolly, J. A. D., et al. (2018). A Geophysical Perspective on the Bulk Composition of Mars. *Journal of Geophysical Research: Planets*, *123*(2), 575–611. https://doi.org/10.1002/2017JE005371

Kovach, R. L., & Watkins, J. S. (1973). The velocity structure of the Lunar crust. *The Moon 7*, 63–75.

Langseth, M. G., Keihm, S. J., & Peters, K. (1976). Revised lunar heat-flow values. *Proc. Lunar Sci. Conf. 7th*, 3143–3171.

Larose, E., Khan, A., Nakamura, Y., & Campillo, M. (2005). Lunar subsurface investigated from correlation of seismic noise. *Geophysical Research Letters*, *32*(16), 1–4. https://doi.org/10.1029/2005GL023518

Lin, F. C., Li, D., Clayton, R. W., & Hollis, D. (2013). High-resolution 3D shallow crustal structure in Long Beach, California: Application of ambient noise tomography on a dense seismic array. *Geophysics*, *78*(4). https://doi.org/10.1190/geo2012-0453.1

Lognonné, P., Banerdt, W. B., Giardini, D., Pike, W. T., Christensen, U., Laudet, P., et al. (2019). SEIS: Insight's Seismic Experiment for Internal Structure of Mars. *Space Science Reviews* (Vol. 215). https://doi.org/10.1007/s11214-018-0574-6

Lognonné, P., Banerdt, W. B., Pike, W. T., Giardini, D., Christensen, U., Garcia, R. F., et al. (2020). Constraints on the shallow elastic and anelastic structure of Mars from InSight seismic data. *Nature Geoscience*, *13*(3), 213–220. https://doi.org/10.1038/s41561-020-0536-y

Mao, S., Campillo, M., van der Hilst, R. D., Brenguier, F., Stehly, L., & Hillers, G. (2019). High Temporal Resolution Monitoring of Small Variations in Crustal Strain by Dense Seismic Arrays. *Geophysical Research Letters*, *46*(1), 128–137. https://doi.org/10.1029/2018GL079944

Nakamura, Y., Latham, G. V., & Dorman, H. J. (1982). Apollo lunar seismic experiment - final summary. *Journal of Geophysical Research*, *87*(Supplement), A117–A123. https://doi.org/10.1029/jb087is01p0a117

Nur, A., & Simmons, G. (1969). The effect of saturation on velocity in low porosity rocks. *Earth and Planetary Science Letters*, *7*(2), 183–193.

https://doi.org/10.1016/0012-821X(69)90035-1

Oren, C., & Nowack, R. L. (2017). Seismic body-wave interferometry using noise autocorrelations for crustal structure. *Geophysical Journal International*, *208*(1), 321–332. https://doi.org/10.1093/gji/ggw394

Panning, M. P., Lognonné, P., Bruce Banerdt, W., Garcia, R., Golombek, M., Kedar, S., et al. (2017). Planned Products of the Mars Structure Service for the InSight Mission to Mars. *Space Science Reviews*, *211*(1–4), 611–650. https://doi.org/10.1007/s11214-016-0317-5

Pasqualini, D., Heitmann, K., TenCate, J. A., Habib, S., Higdon, D., & Johnson, P. A. (2007). Nonequilibrium and nonlinear dynamics in Berea and Fontainebleau sandstones: Low-strain regime. *Journal of Geophysical Research: Solid Earth*, *112*(1), 1–16. https://doi.org/10.1029/2006JB004264

Peng, Z., & Ben-Zion, Y. (2006). Temporal changes of shallow seismic velocity around the Karadere-Düzce branch of the north Anatolian fault and strong ground motion. *Pure and Applied Geophysics*, *163*(2–3), 567–600. https://doi.org/10.1007/s00024-005-0034-6

Phạm, T. S., & Tkalčić, H. (2017). On the feasibility and use of teleseismic P wave coda autocorrelation for mapping shallow seismic discontinuities. *Journal of Geophysical Research: Solid Earth*, *122*(5), 3776–3791. https://doi.org/10.1002/2017JB013975

Prawirodirdjo, L., Ben-Zion, Y., & Bock, Y. (2006). Observation and modeling of thermoelastic strain in Southern California Integrated GPS Network daily position time series. *Journal of Geophysical Research: Solid Earth*, *111*(2), 1–10. https://doi.org/10.1029/2005JB003716

Prieto, G. A., Lawrence, J. F., Chung, A. I., & Kohler, M. D. (2010). Impulse response of civil structures from ambient noise analysis. *Bulletin of the Seismological Society of America*, *100*(5A), 2322–2328. https://doi.org/10.1785/0120090285

Qin, L., Ben-Zion, Y., Bonilla, L. F., & Steidl, J. H. (2020). Imaging and Monitoring Temporal Changes of Shallow Seismic Velocities at the Garner Valley Near Anza, California, Following the M7.2 2010 El Mayor-Cucapah Earthquake. *Journal of Geophysical Research: Solid Earth*, *125*(1), 1–17. https://doi.org/10.1029/2019JB018070

Ratdomopurbo, A., & Poupinet, G. (1995). Monitoring a temporal change of seismic velocity in a volcano: application to the 1992 eruption of Mt. Merapi (Indonesia). *Geophysical Journal International*, *22*(7), 775–778.

Romero, P., & Schimmel, M. (2018). Mapping the Basement of the Ebro Basin in Spain With Seismic Ambient Noise Autocorrelations. *Journal of Geophysical Research: Solid Earth*, *123*(6), 5052–5067. https://doi.org/10.1029/2018JB015498

Rubinstein, J. L. (2011). Nonlinear site response in medium magnitude earthquakes near Parkfield, California. *Bulletin of the Seismological Society of America*, *101*(1), 275–286. https://doi.org/10.1785/0120090396

Shapiro, N. M., & Campillo, M. (2004). Emergence of broadband Rayleigh waves from correlations of the ambient seismic noise. *Geophysical Research Letters*, *31*(7), 8–11. https://doi.org/10.1029/2004GL019491

Smrekar, S. E., Lognonné, P., Spohn, T., Banerdt, W. B., Breuer, D., Christensen, U., et al. (2019). Pre-mission InSights on the Interior of Mars. *Space Science Reviews* (Vol. 215). https://doi.org/10.1007/s11214-018-0563-9

Snieder, R., Grêt, A., Douma, H., & Scales, J. (2002). Coda wave interferometry for estimating nonlinear behavior in seismic velocity. *Science*, *295*(5563), 2253–2255. https://doi.org/10.1126/science.1070015

Suemoto, Y., Ikeda, T., & Tsuji, T. (2020). Temporal Variation and Frequency Dependence of Seismic Ambient Noise on Mars From Polarization Analysis. *Geophysical Research Letters*, *47*(13), 1–9. https://doi.org/10.1029/2020GL087123

Tanimoto, T., Eitzel, M. V., & Yano, T. (2008). The noise cross-correlation approach for Apollo 17 LSPE data: Diurnal change in seismic parameters in shallow lunar crust. *Journal of Geophysical Research E: Planets*, *113*(8), 1–12. https://doi.org/10.1029/2007JE003016

TenCate, J. A., Pasqualini, D., Habib, S., Heitmann, K., Higdon, D., & Johnson, P. A. (2004). Nonlinear and nonequilibrium dynamics in geomaterials. *Physical Review Letters*, *93*(6), 4–7. https://doi.org/10.1103/PhysRevLett.93.065501

Tsai, V. C. (2011). A model for seasonal changes in GPS positions and seismic wave speeds due to thermoelastic and hydrologic variations. *Journal of Geophysical Research: Solid Earth*, *116*(4), 1–9. https://doi.org/10.1029/2010JB008156

Wang, B., Yang, W., Wang, W., Yang, J., Li, X., & Ye, B. (2020). Diurnal and Semidiurnal P- and S-Wave Velocity Changes Measured Using an Airgun Source. *Journal of Geophysical Research: Solid Earth*, *125*(1). https://doi.org/10.1029/2019JB018218

Yang, C., Li, G., Niu, F., & Ben-Zion, Y. (2019). Significant Effects of Shallow Seismic and Stress Properties on Phase Velocities of Rayleigh Waves Up to 20 s. *Pure and Applied Geophysics*, *176*(3), 1255–1267. https://doi.org/10.1007/s00024-018-2075-7

Yoder, C. F., Konopliv, A. S., Yuan, D. N., Standish, E. M., & Folkner, W. M. (2003). Fluid core size of Mars from detection of the solar tide. *Science*, *300*(5617), 299–303. https://doi.org/10.1126/science.1079645

Figure captions

Figure 1. (a). Waveforms with 100 Hz sampling rate after removing the linear trend. Relative amplitudes of the three component seismic data are preserved. (b). Spectrogram of the waveform at EW component. (c). Wind (colored dots) and temperature (black dashed curve) recordings during Julian days 66-67 (UTC on Earth). Black ticks on x-axis correspond to UTC on Earth, while the local mean solar time on Mars is shown in red with a format of "dddThh". The first three digits ("ddd") represent the Julian day and the last two digits (hh) indicate the local time in hours on Mars.

Figure 2. Results from the two-day 100 Hz data: (a). ACFs of EW component waveforms. (b). Envelope functions of EW-component ACFs. (c). The reference (dashed curve) and example (solid curve) ACFs from EW (top), NS (center) and UD (bottom) components. The reference ACF denotes the stack of all ACFs, and the example ACF is calculated at 1 pm of Julian day 66 (UTC on Earth). Vertical blue lines indicate the cross-correlation time windows. (d). Stacked envelope functions at EW (black), NS (red) and vertical (blue) components. T_1, T_2 and T_3 denote the time of the second, third and fourth peaks in the stacked envelope functions, respectively. Horizontal bars indicate the cross-correlation time windows, same as the vertical blue lines in (c).

Figure 3. dt/t measurements (colored dots) for 100 Hz data at EW (top), NS (center) and vertical (bottom) components, colored by the cross-correlation coefficients. The red curve illustrates the smoothed dt/t data using a running window of 65 points. The

linearly scaled temperature curve (black), $g_0(T; a, b)$, has maximum and minimum values that match the median of the upper 95 and lower 5 percentiles of the red curve. The vertical purple dashed lines indicate the Martian day time (8:00 am to 8:00 pm) when the difference between the two curves is large. Ticks on x-axis are formatted similarly as in Fig. 1.

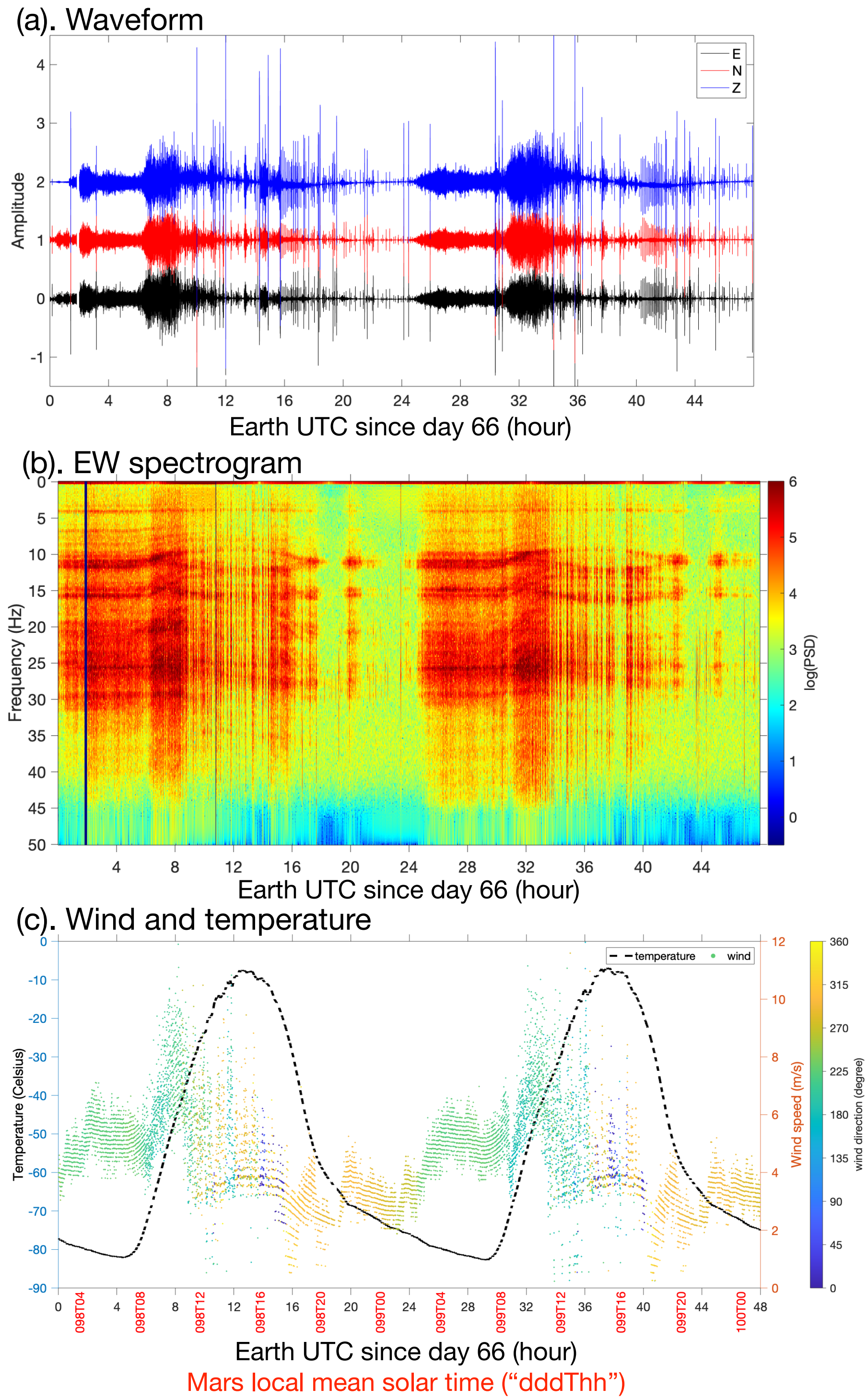

Figure 1. (a). Waveforms with 100 Hz sampling rate after removing the linear trend. Relative amplitudes of the three component seismic data are preserved. (b). Spectrogram of the waveform at EW component. (c). Wind (colored dots) and temperature (black dashed curve) recordings during Julian days 66-67 (UTC on Earth). Black ticks on x-axis correspond to UTC on Earth, while the local mean solar time on Mars is shown in red with a format of “dddThh”. The first three digits (“ddd”) represent the Julian day and the last two digits (hh) indicate the local time in hours on Mars.

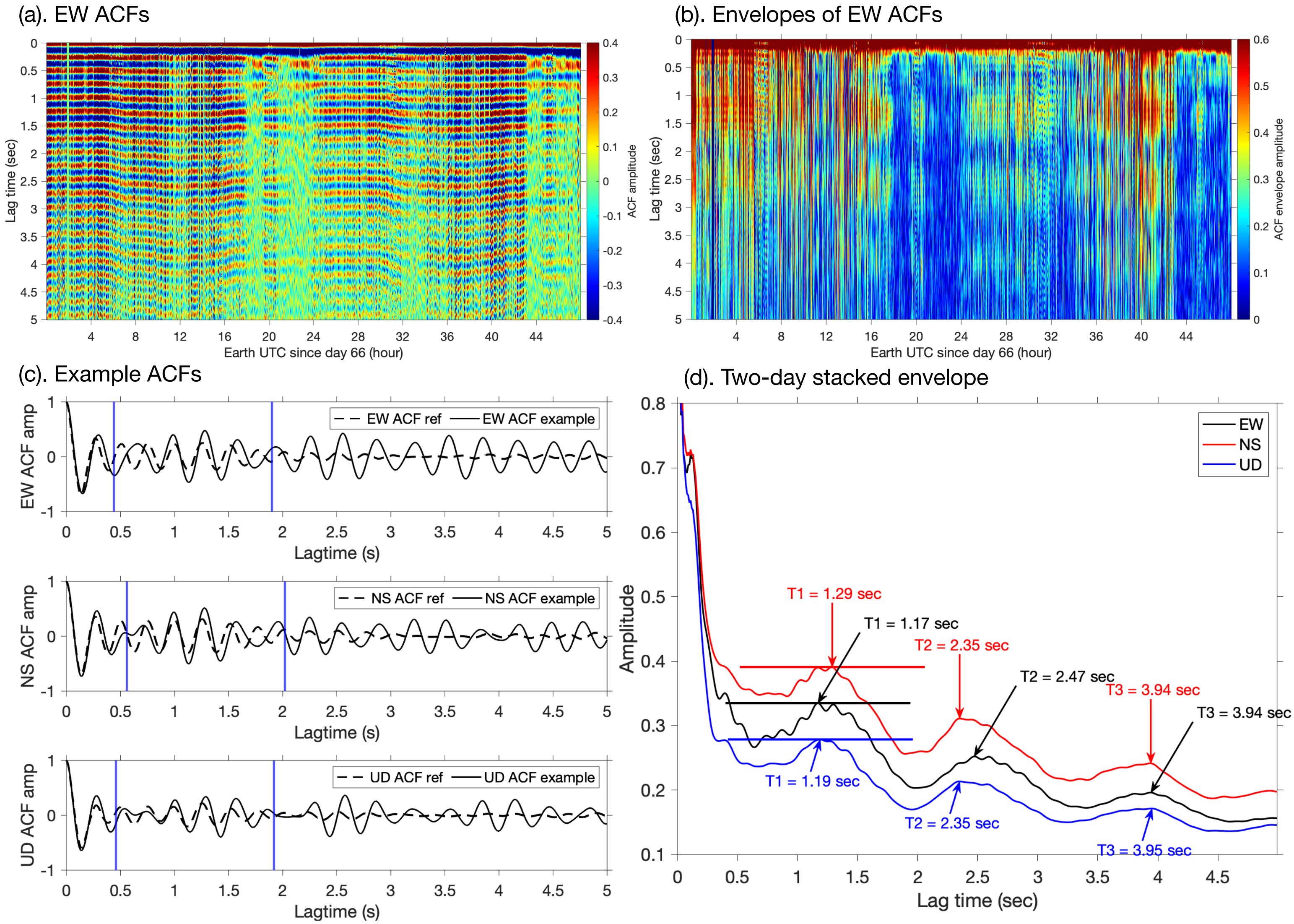

Figure 2. Results from the two-day 100 Hz data: (a). ACFs of EW component waveforms. (b). Envelope functions of EW-component ACFs. (c). The reference (dashed curve) and example (solid curve) ACFs from EW (top), NS (center) and UD (bottom) components. The reference ACF denotes the stack of all ACFs, and the example ACF is calculated at 1 pm of Julian day 66 (UTC on Earth). Vertical blue lines indicate the cross-correlation time windows. (d). Stacked envelope functions at EW (black), NS (red) and vertical (blue) components. T_1, T_2 and T_3 denote the time of the second, third and fourth peaks in the stacked envelope functions, respectively. Horizontal bars indicate the cross-correlation time windows, same as the vertical blue lines in (c).

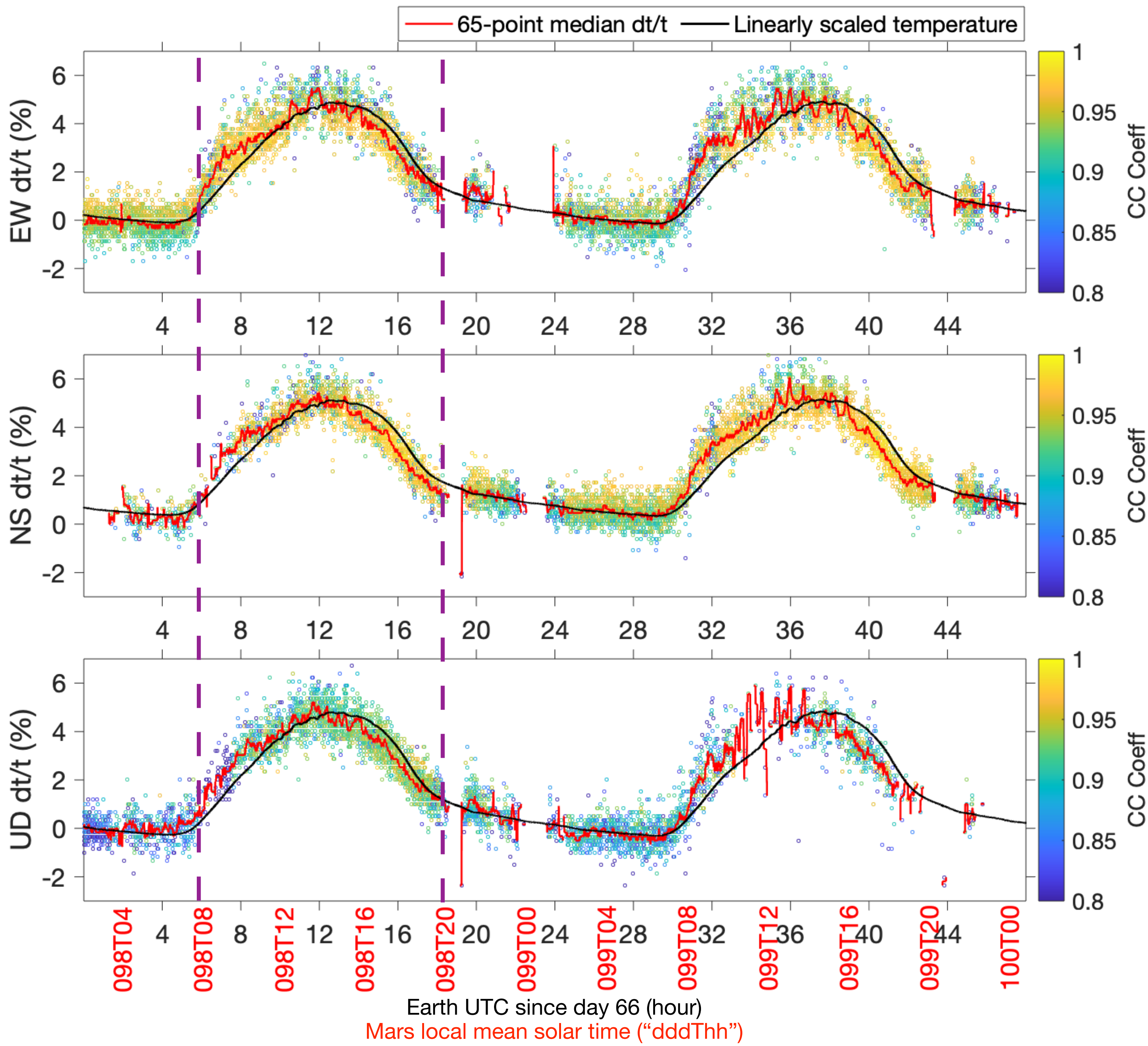

Figure 3. dt/t measurements (colored dots) for 100 Hz data at EW (top), NS (center) and vertical (bottom) components, colored by the cross-correlation coefficients. The red curve illustrates the smoothed dt/t data using a running window of 65 points. The linearly scaled temperature curve (black), $g_0(T; a, b)$, has maximum and minimum values that match the median of the upper 95 and lower 5 percentiles of the red curve. The vertical purple dashed lines indicate the Martian day time (8:00 am to 8:00 pm) when the difference between the two curves is large. Ticks on x-axis are formatted similarly as in Fig. 1.